Computers and Geotechnics 119 (2020) 103383

Contents lists available at ScienceDirect

Computers and Geotechnics

journal homepage: www.elsevier.com/locate/compgeo

Research Paper

Practical nonlinear constitutive model for rockfill materials with application to rockfill dam

Si-hong Liu[a], Yi Sun[a,*], Chao-min Shen[a], Zhen-Yu Yin[b]

[a] College of Water Conservancy and Hydropower Engineering, Hohai University, Nanjing 210098, China
[b] Department of Civil and Environmental Engineering, The Hong Kong Polytechnic University, Hung Hom, Kowloon, Hong Kong

ARTICLE INFO

Keywords:
Rockfill materials
Dilatancy
Intermediate principal stress
Nonlinear constitutive model

ABSTRACT

In this paper, a nonlinear constitutive model for rockfill materials is proposed to account for the coupling influence of the mean effective stress *p* and the deviatoric stress *q* on the deformation of rockfill materials. In the model, the stress-dilatancy relationship derived from the microstructural changes of granular materials is adopted, and the strength nonlinearity of rockfill materials is considered by using a logarithmic relationship between the peak friction angle and the mean effective stress. The SMP criterion is incorporated into the model to consider the influence of the intermediate principal stress. The good performance of the proposed model is demonstrated through modelling triaxial tests on rockfill materials from a rockfill dam. In addition, the FEM simulated deformation of a real CFRD using the proposed model agrees well with the monitored data.

1. Introduction

Rockfill dams have been widely adopted due to the inherent flexibility and adaptability to different foundation conditions. In addition, due to the increasing construction technology, the rockfill dams have become the most economical dam type. As the main component of the dams, rockfill materials is of profound importance to the stability and the safe operation of the dams. In general, the strength and deformation properties of rockfill materials are very complicated [1–4]. For example, peak shear strength decreases with the confining stress increasing, exhibiting a non-linear function of confining stress; shear induced volume deformation (contraction or dilatation) is not negligible. Apparently, an ideal constitutive modelling of rockfill materials need reasonably reflect these complex behaviors.

So far, many constitutive models for rockfill materials have been developed. These models can be classified as (1) nonlinear hypoelastic models [5,6], (2) incrementally nonlinear models [7,8], (3) elastoplastic models [9–17], (4) hypoplastic models [18–21], and (5) micromechanics-based models [22–25]. In general, the first four categories are phenomenological models, which are commonly adopted in engineering practice due to their efficiency in finite-element analyses.

Nonlinear hypoelastic models, especially Duncan-Chang Model [5] and K-G models [6,26–28], are mostly adopted in the finite-element analyses of rockfill dams owing to the simplicity and easily-understandable concept of the models. However, the Duncan-Chang Model cannot take the influence of the intermediate principal stress into consideration as the Mohr-Coulomb failure criterion of soils is used. Moreover, the dilatancy of rockfill materials cannot be reflected in the model as the shear-induced volume change is not considered. As a result, the Duncan-Chang Model sometimes overestimates the settlements of rockfill dams when it is adopted in the finite element analysis for rockfill dams, especially for medium and low dams. Domaschuk and Villiappan firstly proposed a K-G model in 1975 [6], and later many improvements [26–28] have been made to describe the coupling influences of mean effective stress *p* and deviatoric stress *q* on the deformation of rockfill material.

This paper presents a simple nonlinear constitutive model for rockfill materials that can consider the coupling influence of the mean effective stress *p* and the deviatoric stress *q* and the influence of the intermediate principal stress on the deformation of rockfill materials. The determination method for the model parameters is suggested. Afterwards, the proposed constitutive model is adopted in finite element method to simulate the deformation of a real concrete-faced rockfill dam (CFRD) with adequate monitoring data.

2. Nonlinear constitutive model

2.1. Framework of the model

In this study, a nonlinear hypoelastic constitutive model for rockfill

* Corresponding author.
E-mail address: sunyihhu@163.com (Y. Sun).

https://doi.org/10.1016/j.compgeo.2019.103383
Received 10 July 2019; Received in revised form 20 August 2019; Accepted 2 December 2019

materials attempts to be developed. In the constitutive modeling, the general relationship between incremental strains and incremental stresses is given by

$$d\varepsilon_{kl} = C_{ijkl}(\sigma_{mn})d\sigma_{kl} \tag{1}$$

where C_{ijkl} are complementary constitutive tensors (or moduli) that are stress level dependent. The stress-strain behavior is more conveniently described using the parameters p, q, ε_v and ε_s defined as

$$\left.\begin{array}{c} p = \frac{(\sigma_1+\sigma_2+\sigma_3)}{3} \\ q = \frac{1}{\sqrt{2}}\sqrt{(\sigma_1-\sigma_2)^2+(\sigma_2-\sigma_3)^2+(\sigma_3-\sigma_1)^2} \\ \varepsilon_v = \varepsilon_1+\varepsilon_2+\varepsilon_3 \\ \varepsilon_s = \frac{\sqrt{2}}{3}\sqrt{(\varepsilon_1-\varepsilon_2)^2+(\varepsilon_2-\varepsilon_3)^2+(\varepsilon_3-\varepsilon_1)^2} \end{array}\right\} \tag{2}$$

In p-q stress space, Eq. (1) can be derived as

$$d\varepsilon_v = \frac{dp}{K} + \frac{dq}{J_1} \tag{3a}$$

$$d\varepsilon_s = \frac{dp}{J_2} + \frac{dq}{G} \tag{3b}$$

where K is a bulk modulus, representing the volumetric stiffness with respect to dp; J_1 is a shear dilatancy modulus (coupling modulus), accounting for the volumetric strain produced by an increment dq; G is a shear modulus that controls shear strain with respect to dq; and J_2 is another coupling modulus, accounting for the shear strain produced by an increment dp. Generally, the coupling moduli J_1 and J_2 are different, and it's not easy to determine them separately from experimentally observed stress-strain data. For the sake of simplicity, either $J_2 = \infty$ or $J_1 = J_2 = J$ was assumed by some scholars [26,28]. For the assumption of $J_2 = \infty$, the model cannot incorporate shear strains generated by changes in mean effective stress p. Also, the assumption of $J_2 = \infty$ leads to the non-symmetry of the general matrix of the model. As a result, it is difficult to use some existing efficient linear equation solvers in FEM. These two shortcomings can be avoided in the assumption of $J_1 = J_2 = J$. Therefore, this paper adopted the assumption of $J_1 = J_2 = J$, that is to say, the $dp - d\varepsilon_s$ coupling and the $dq - d\varepsilon_v$ coupling are controlled by the same J modulus. Positive dilatancy, that is, expansion during shearing, is associated with $J < 0$. Compression during shearing produces $J > 0$.

2.2. Derivation of hypoelastic K, G and J modulus functions

2.2.1. Bulk modulus K

The bulk modulus K relates the volumetric strain ε_v to the mean effective stress p, which is commonly determined though isotropic compression tests. The results of isotropic compression tests on rockfill materials indicate that the relationship between the volumetric strain ε_v and the mean effective stress p is more reasonably expressed with an exponential function [29]

$$\varepsilon_v = C_t\left[\left(\frac{p}{P_a}\right)^n - \left(\frac{p_0}{P_a}\right)^n\right] \tag{4}$$

where C_t, n are the parameters fitting experimentally observed stress-strain data; p_0 is an isotropically initial stress and p_a is the atmospheric pressure.

Differentiating Eq. (4) yields

$$d\varepsilon_v = C_t n(\frac{p}{P_a})^{n-1}\frac{dp}{P_a} \tag{5}$$

Then, the bulk modulus K can be obtained from its definition

$$K = \frac{dp}{d\varepsilon_v} = \frac{P_a}{C_t n}(\frac{p}{P_a})^{1-n} \tag{6}$$

Assuming that $K_b = 1/(C_t n)$ and $n_1 = 1 - n$, Eq. (6) is rewritten as

$$K = K_b P_a\left(\frac{p}{P_a}\right)^{n_1} \tag{7}$$

2.2.2. Shear modulus G and coupling modulus J

It is noted that the shear modulus G in Eq. (3b) controls the shear strain with respect to dq under dp = 0. Ideally, it should be determined from the shear tests under the constant mean effective stress p, which are seldom carried out in practice. Usually, conventional triaxial tests are carried out to determine the model parameters. Therefore, before giving the expression for G, we define first the shear modulus determined from conventional triaxial tests as G_{TC}.

Rockfill materials exhibit a nonlinear frictional behavior with an asymptotic relationship between the deviatoric stress q and the shear strain ε_s. Here, the $q - \varepsilon_s$ relation measured in conventional triaxial tests is supposed to be fitted with a hyperbolic function, expressed as

$$q = \frac{\varepsilon_s}{a + b\varepsilon_s} \tag{8}$$

where a and b are the constants whose values can be determined experimentally. To be more specific, they can be related to the initial tangential shear modulus G_{TCi} ($a = 1/G_{TCi}$) and the asymptotic value q_{ult} of the deviatoric stress q where the curve $q - \varepsilon_s$ approaches at infinite strain ($b = 1/q_{ult}$), respectively.

It is commonly found that the asymptotic value of the deviatoric stress q is larger than the shear failure strength q_f by a small amount. This would be expected, because the hyperbola remains below the asymptote at all finite values of strain. The asymptotic value q_{ult} may be related to the shear failure strength q_f, however, by means of a factor R_f as shown by

$$q_f = R_f q_{ult} \tag{9}$$

Under the triaxial condition, the shear modulus $G_{TC} = dq/d\varepsilon_s$ by the definition, can be obtained by differentiating Eq. (8) and combining Eq. (9):

$$G_{TC} = \frac{dq}{d\varepsilon_s} = \frac{1}{a}[1 - bq]^2 = G_{TCi}(1 - R_f\frac{q}{q_f})^2 \tag{10}$$

Experimental studies have shown that the initial tangential shear modulus G_{TCi} varies with the mean effective stress p. Referring to Janbu's study [30], it may be expressed as

$$G_{TCi} = K_G P_a\left(\frac{p}{P_a}\right)^{n_2} \tag{11}$$

where K_G is a material modulus, and n_2 is the exponent determining the rate of variation of G_{TCi} with p. Both K_G and n_2 are dimensionless and may be determined readily from the results of a series of triaxial tests by plotting the values of G_{TCi} against p on log-log scales and fitting a straight line to the data.

In Eq. (10), the shear failure strength q_f is usually related to the mean effective stress p, which depends on the failure criterion. The criterion of the Extended Mises type $q_f = M_f p$ was adopted for the shear yield and shear failure of soils in the Cam-clay model, and many other models, where $M_f = 6\sin\varphi/(3 - \sin\varphi)$ under the triaxial condition (φ is the peak friction angle). If the criterion of the Extended Mises type is adopted, substituting Eq. (11) into Eq. (10) yields

$$G_{TC} = K_G P_a\left(\frac{p}{P_a}\right)^{n_2}\left(1 - R_f\frac{q}{M_f p}\right)^2 \tag{12}$$

However, as exprimental evidence shows, the Extended Mises criterion grossly overestimates strength in triaxial extension, and also results in incorrect intermediate stress ratios in π plane. It is known that the failure of soil can be reasonably explained by the SMP criterion [31], which is written as

$$\frac{\tau_{SMP}}{\sigma_{SMP}} = \sqrt{\frac{I_1 I_2 - 9I_3}{9I_3}} = const \tag{13}$$

where τ_{SMP} and σ_{SMP} are the shear and normal stresses on the SMP, and I_1, I_2 and I_3 are the first, second and third stress invariants.

In this study, we adopt the SMP criterion instead of the Extended Mises criterion. To this end, the transformed stress tensor $\tilde{\sigma}_{ij}$ proposed by Yao et al. [11,12] is used, which can transform the SMP criterion into an Extended Mises type criterion in the new stress transformed stress space. The transformed stress tensor $\tilde{\sigma}_{ij}$ is expressed as

$$\left.\begin{aligned} \tilde{\sigma}_{ij} &= p\delta_{ij} + \frac{q_c}{q}(\sigma_{ij} - p\delta_{ij}) \\ q_c &= \frac{2I_1}{3\sqrt{(I_1I_2 - I_3)/(I_1I_2 - 9I_3)} - 1} \end{aligned}\right\} \tag{14}$$

By using the transformed stress tensor $\tilde{\sigma}_{ij}$, the SMP criterion can be expressed as

$$\tilde{q}_f = M_f \tilde{p} \tag{15}$$

Matsuoka et al. [32] introduced the SMP criterion into the Cam-clay model by replacing the stress tensor σ_{ij} with the transformed stress tensor $\tilde{\sigma}_{ij}$. Similarly, the SMP criterion (Eq. (15)) is incorporated into the shear modulus of Eq. (12) through $\tilde{\sigma}_{ij}$, leading to

$$G_{TC} = K_G P_a \left(\frac{\tilde{p}}{P_a}\right)^{n_2} \left(1 - R_f \frac{\tilde{q}}{M_f \tilde{p}}\right)^2 \tag{16}$$

By considering $G_{TC} = dq/d\varepsilon_s$, Eq. (3b) can be rewritten as

$$\frac{1}{G_{TC}} = \frac{1}{J}\frac{dp}{dq} + \frac{1}{G} \tag{17}$$

Combining Eq. (3a) and Eq. (3b), one can obtain

$$\frac{d\varepsilon_v}{d\varepsilon_s}\left(\frac{1}{J} + \frac{1}{G}\frac{dq}{dp}\right) = \frac{1}{K} + \frac{1}{J}\frac{dq}{dp} \tag{18}$$

Assuming $\xi = dq/dp$ and $D = d\varepsilon_v/d\varepsilon_s$, we can derive the shear modulus G and the coupling modulus J from Eqs. (17) and (18).

$$G = \frac{KG_{TC}\xi^2}{K\xi^2 - DK\xi + G_{TC}} \tag{19}$$

$$J = \frac{K\xi G_{TC}}{DK\xi - G_{TC}} \tag{20}$$

Fig. 1 gives the typical stress-strain relation of granular materials during shearing in a triaxial test. It demonstrates that the sample is usually compressive at the beginning of shearing and gradually turns to be dilative. The stress ratio $\eta(=q/p)$ corresponding to the phase transformation point from contraction to dilatation is denoted as M, which can be related to the phase transformation friction angle ψ with $M = 6\sin\psi/(3 - \sin\psi)$. Considering this typical stress-strain characteristic and the microstructure change of granular materials, Liu et al. [33] proposed a stress-dilatancy equation, expressed as

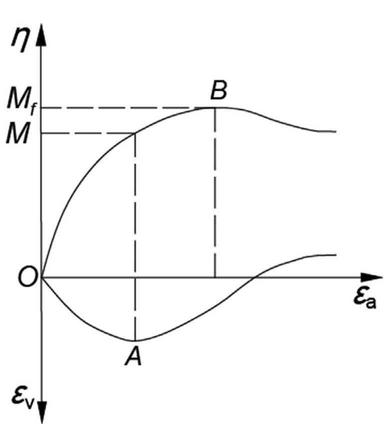

Fig. 1. Typical stress-strain relationship of coarse granular materials.

$$D = \frac{d\varepsilon_v}{d\varepsilon_s} = \frac{mM^{m+1} - m\eta^{m+1}}{(m+1)\eta^m} \tag{21}$$

where $\eta = q/p$, and m is an experimentally fitting constant. Eq. (21) can reasonably describe the volumetric change of granular materials from the initial compression ($d\varepsilon_v > 0$ when $0 < \eta < M$) to the positive dilatancy ($d\varepsilon_v < 0$ when $M < \eta$). It can be regarded as a general form of several exsiting stress-dilatancy equations. For instance, when $m = 1$, Eq. (21) is degenerated into the dilatancy equation as used in the modified Cam-clay model. The first-order Taylor expansion of Eq. (21) at $\eta = M$ leads to a dilatancy equation as used in the generalized plasticity model for sands, proposed by Pastor and Zienkiewicz [34].

Eqs. (7), (19) and (20) provide a straightforward way of obtaining three moduli K, G and J from experimental data. In this nonlinear constitutive model, the SMP criterion is incorporated in the shear modulus G_{TC} and therewith the moduli G and J to reflect the influence of the intermediate principal stress. The coupling modulus J accounts for the volumetric strain produced by an increment dq in deviatoric (shear) stress, and also the shear strain produced by an increment dp in mean effective stress. The dilatancy of coarse granular materials is considered in the model by adopting a stress-dilatancy equation of Eq. (21) in the moduli G and J. The great advantage of this model is its simplicity. It is noted from the above derivation of the moduli that this simple model does not deal with the mechanical behavior of granular materials after their peak shear strengths. However, the proposed model should be sufficient to be applied in the rockfill dam engineering because most of rockfill dams operate under a relatively lower stress level [35–38].

2.3. Nonlinearity of shear strength

Shear strengths of rockfill materials often exhibit nonlinearity under different mean effective stresses, mainly resulting from particle breakage. The strength nonlinearity can be described by the functional relationship between the peak friction angle φ and the mean effective stress p.

$$\varphi = \varphi_0 - \Delta\varphi \lg\left(\frac{p}{P_a}\right) \tag{22}$$

where φ_0 is the peak friction angle when the mean effective stress is equal to the atmospheric pressure p_a; $\Delta\varphi$ represents the reduction magnitude of the peak friction angle per unit increase of the order of magnitude of the mean effective stress.

Similarly, it is assumed that the relationship between the internal friction angle at the phase transformation point ψ and the mean effective stress p is described by

$$\psi = \psi_0 - \Delta\psi \lg\left(\frac{p}{P_a}\right) \tag{23}$$

where ψ_0 is the internal friction angle at the phase transformation point when $p = p_a$; $\Delta\psi$ is the change of the internal friction angle ψ when the mean effective stress increases by one order of magnitude.

Normally, the above-mentioned friction angle parameters (φ_0, $\Delta\varphi$, ψ_0, $\Delta\psi$) can be determined by triaxial compression tests.

2.4. Determination of model parameters

The model includes ten parameters of K_b, n_1, K_G, n_2, R_f, m, φ_0, $\Delta\varphi$, ψ_0, $\Delta\psi$, which can be determined by a series of conventional tests. The compression parameters (K_b, n_1) can be determined by an isotropic compression test through fitting $\varepsilon_v - p$ curve, while other parameters can be calibrated from conventional triaxial tests. The shear parameters (K_G, n_2, R_f) can be obtained

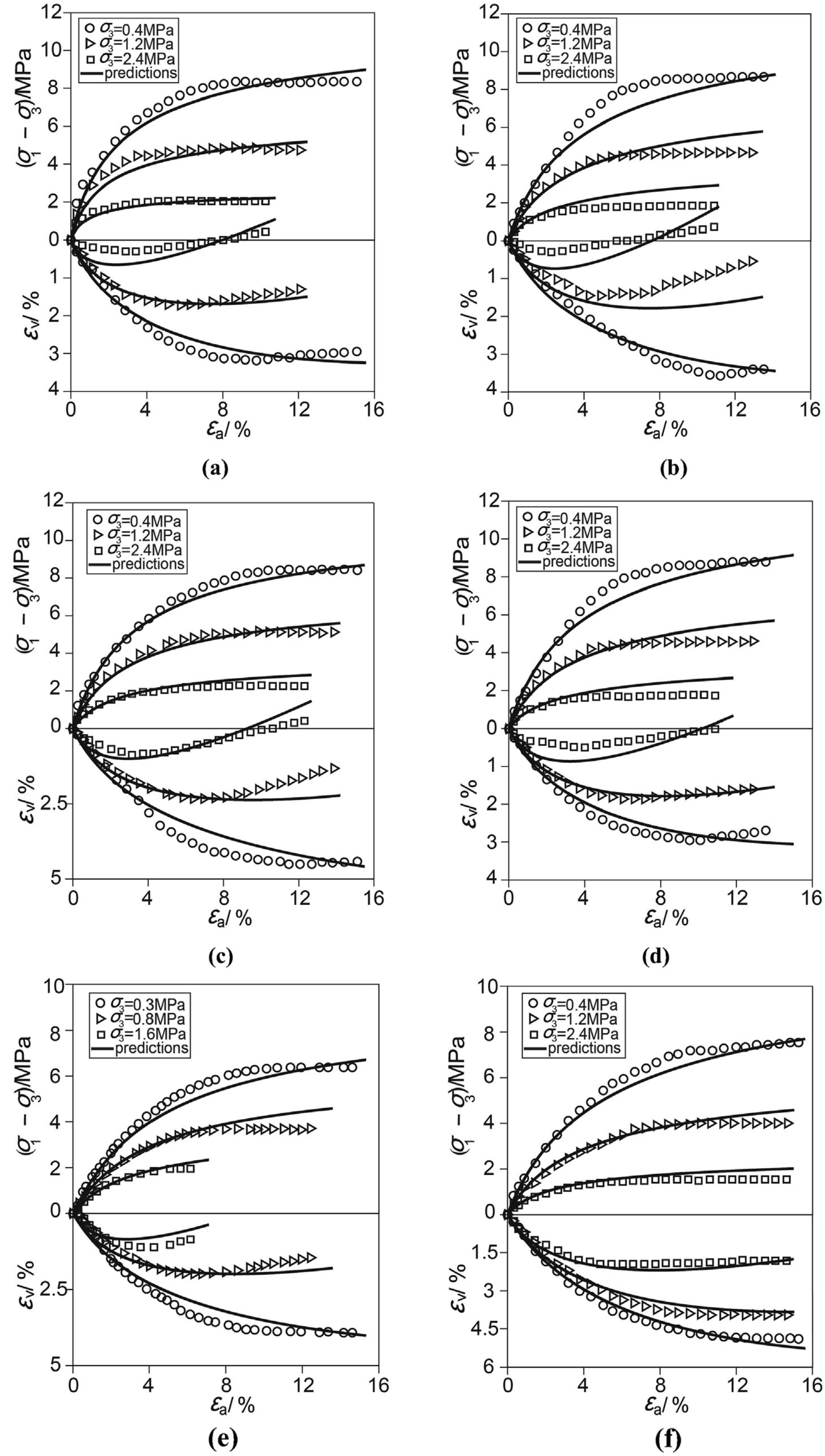

Fig. 2. Comparison between experimental and predicted results of triaxial tests on Tankeng CFRD materials: (a) Cushion; (b) Transition; (c) Rockfill I; (d) Gravel; (e) Rockfill II; (f) Alluvium (Sand gravel).

Table 1
The nonlinear model parameters for different materials of Tankeng CFRD.

Material	Dry density (kN/m^3)	m	φ_0	$\Delta\varphi$	ψ_0	$\Delta\psi$	K_b	n_1	K_G	n_2	R_f
Cushion	22	0.75	57.0°	11.8°	43.7°	1.4°	129	0.33	1515	0.42	0.79
Transition	21.5	0.72	50.7°	11.7°	43.9°	1.2°	513	0.16	1452	0.38	0.63
Rockfill I	21.2	0.85	51.3°	12.2°	44.7°	1.2°	380	0.15	1288	0.46	0.65
Gravel	21.5	0.67	51.7°	10.2°	44.8°	1.7°	717	0.19	1099	0.48	0.71
Rockfill II	20.7	0.71	53.2°	12.5°	47.1°	1.7°	176	0.58	1369	0.31	0.63
Alluvium	20.2	0.86	52.8°	6.3°	46.2°	3.5°	126	0.19	821	0.44	0.89

by fitting the curve $q - \varepsilon_s$ of the drained tests under different confining stresses, and the stress-dilatancy parameter (m) can be measured based on the experimental $D - \eta$ curve. The peak friction angle and the phase transformation friction angle φ and ψ can be determined from the stress ratios at the peak stress state and phase transformation state using $M_f = 6\sin\varphi/(3 - \sin\varphi)$ and $M = 6\sin\psi/(3 - \sin\psi)$, respectively. The friction angle parameters (φ_0, $\Delta\varphi$, ψ_0, $\Delta\psi$) can be obtained by fitting the curves $\varphi - p$ and $\psi - p$.

2.5. Experimental verification

A series of drained triaxial tests have been conducted on the construction materials and the site alluvium of the Tankeng CFRD that are described in detail in Section 3.1. The triaxial test results in Fig. 2 demonstrate that the shearing dilatation is more significant under low confining pressures compared to under high confining stresses. They are simulated using the proposed model with the set of model parameters listed in Table 1. As shown in Fig. 2, the model responses are broadly in good agreement with the experimental data, indicating the performance of the proposed model with the simplification ($J_1 = J_2 = J$) and the stress-dilatancy equation proposed by Liu et al. [33].

3. Application

3.1. The Tankeng project

As an example, the proposed nonlinear constitutive model was applied in the FEM analysis of the Tankeng concrete-faced rockfill dam (CFRD). The Tankeng CFRD of 162 m in height, is located on the middle reaches of the Oujiang River, Zhejiang Province, China. The layout of the dam is shown in Fig. 3. The dam crest is 505 m long and 12 m wide. The upstream concrete face is composed of into 42 slabs. Each slab is 12 m wide and the adjacent slabs are waterproofed with vertical joints. The slabs are connected to the toe slabs located on the abutments through peripheral joints.

Fig. 4 shows the typical cross-section of the dam corresponding to section I-I in the layout. The upstream and downstream slopes of the dam are 1:1.4 and 1:1.55 (average), respectively. The thickness d of the concrete face slab is 0.3 m at the top elevation of 167 m and varies linearly with a function of $d = 0.3 + 0.0035H$ downwards the slope, where H is the vertical distance to the top elevation of 167 m. Behind the concrete face slab, a cushion zone with a horizontal width of 3.0 m is placed, which is composed of sands and gravels with a maximum grain size of 6 cm. Between the cushion zone and the main rockfill zone, a 5.0 m horizontally wide transition zone with a maximum grain size of 30 cm is provided to prevent fine particles of the cushion zone from entering the pores of the rockfill. The main dam body consists of rockfill I, gravel and rockfill II zones. The rockfill I zone provides a support for

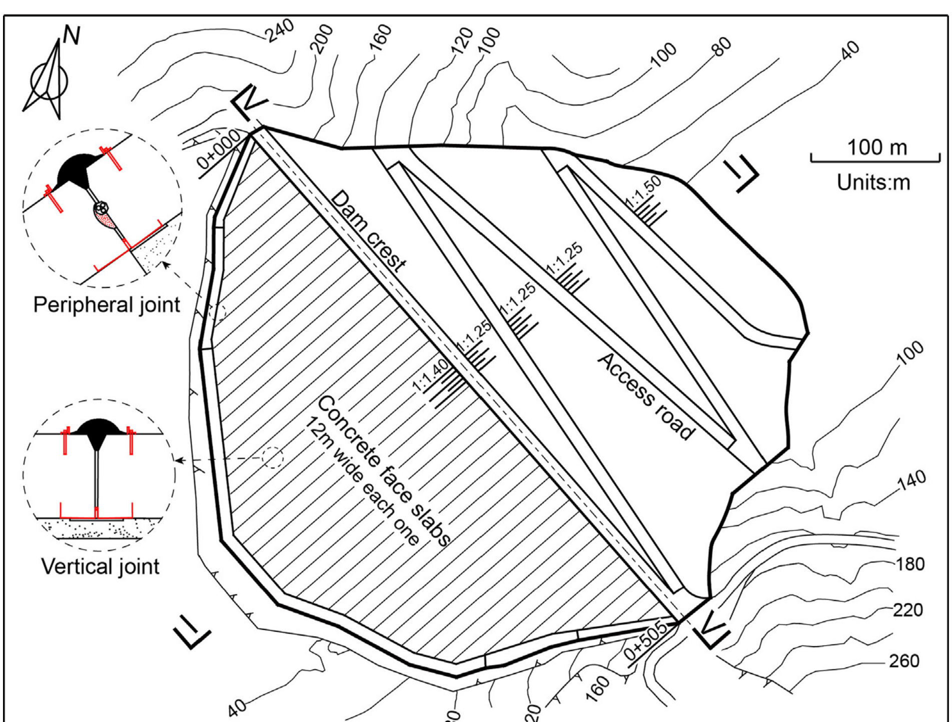

Fig. 3. Layout of the Tankeng CFRD.

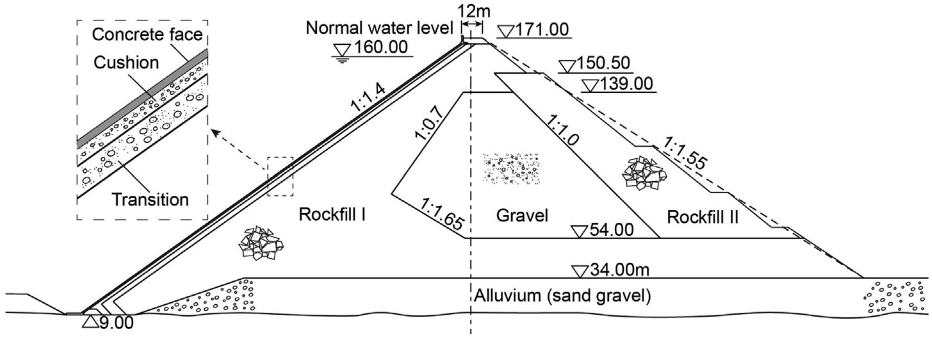

Fig. 4. Typical cross section of Tankeng CFRD.

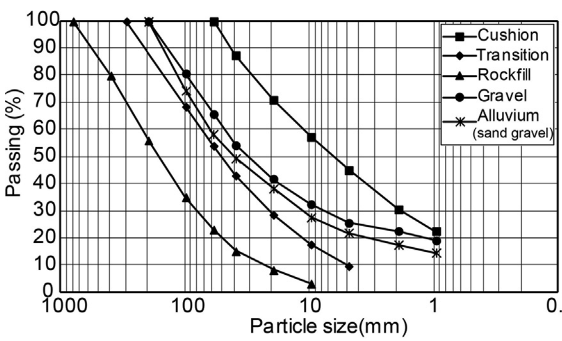

Fig. 5. Gradation curves of alluvium and dam construction materials.

hydrostatic loads transmitted from the cushion zone and transition zone. The gravel zone is surrounded by rockfill I and II zones since it has relatively lower shear strength. The dam foundation has 20–30 m thick alluvium of sand gravels. The gradations of the dam construction materials and the foundation alluvium are given in Fig. 5.

3.2. FE analysis model

Fig. 6 presents the FE model for the Tankeng dam considering the construction and the first impounding sequence. It is noted that the FE model contains the foundation alluvium and the bottom of the alluvium layer is vertically restrained in the calculation. The construction stage was simulated by 13 loading steps following exactly the construction procedure of the project (1–11, 13–14 steps). The hydrostatic load was applied on the upstream surface in 2 steps (12, 15 steps), in accordance with the reservoir level records, to reflect the impact of the first impounding and water level fluctuation during 2008–2012. In summary, the three-dimensional FE model contains 7162 eight-node elements, 15 loading steps and six rockfill materials.

The rockfill materials of the Tanleng CFRD were described using the proposed nonlinear model, and the model parameters are listed in Table 1. The concrete face slab was described using the linear elastic model with an elastic module of 30 GPa, Poisson's ratio of 0.167 and density of 25 kN/m^3. The interface between the concrete face slab and the cushion layer was described using Goodman elements and the tangential stress-displacement relationship at the interface was characterized by the Clough-Duncan model, the details of which were seen in [39–41]. The parameters of the Clough-Duncan model K_0, n, R_f and φ adopted in the calculation are 3500, 0.56, 0.74 and 36°, respectively. The vertical and peripheral joints were simulated using a pair of nodes that can be combined into a single node due to compressive stress application and separated into two independent nodes due to tensile stress application.

In 3D FE analysis, the constitutive relation is usually expressed in Voigt stress space, which has been given in Appendix A for the proposed constitutive model. A incremental algorithm is used to solve non-linear finite element equations and a symmetric successive over relaxation (SSOR) method is used to solve finite element control equation in this FE analysis.

3.3. Results and discussion

Fig. 7 shows the contours of the calculated dam body deformation at the maximum cross section after the first impounding. It can be seen

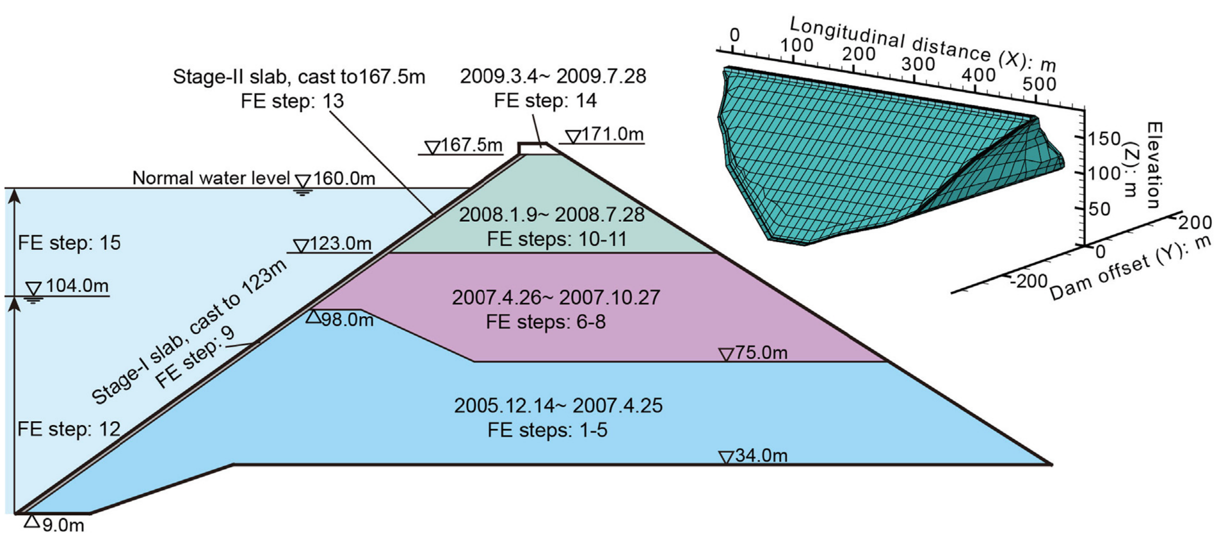

Fig. 6. Construction stages and three-dimensional mesh of Tankeng CFRD.

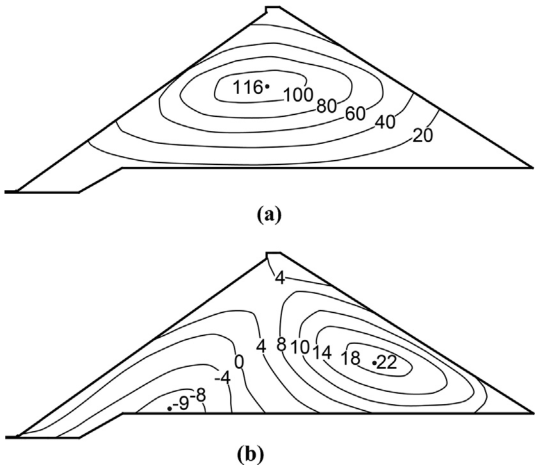

Fig. 7. Contours of the calculated deformation of the dam body at the maximum section after the first impounding (unit: cm).

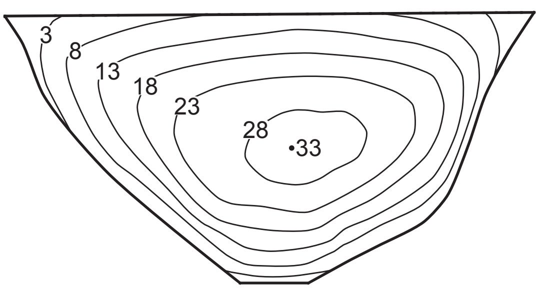

Fig. 8. Contours of the calculated concrete face slab deflection after the first impounding (unit: cm).

that the maximum settlement occurred nearly in half of the dam height (Fig. 7a). The maximum settlement of 116 cm accounts for 0.72% of the dam height, which is within the range as observed in most of CFRDs [37]. Under the action of the water pressure on the upstream concrete face slabs, the overall trend of the horizontal displacement is towards the downstream with the maximum magnitude of 22 cm at the downstream (Fig. 7b). Fig. 8 presents the contours of the calculated concrete face slab deflection after the first impounding. The maximum deflection is 33 cm, occurring in the middle of the upstream face slabs. Reference [37] presents the face slab deflection measured in the 87 case histories with respect to dam heights. Statistical results show that the face slab deflection in most cases is less than 0.40% of the dam height, and more than half cases are less than 0.2% of the dam height. Very few cases that were constructed using low-strength rockfills exhibit the face slab deflection values up to 0.6% of the dam height. The calculated face slab deflection 33 cm of the Tangken CFRD accounts for 0.2% of the dam height, within the range of the statistical results for most of CFRDs [37]. Fig. 9 compares the calculated dam settlement and the slab deflection with the monitored data at the maximum cross-section after the first impounding. The settlement at the monitoring point V3-2 was not measured because the monitoring gauge had been damaged before the completion of the dam. Anyway, it can be observed that both the calculated settlements of the dam and the calculated deflection of the concrete face slab agree basically with the monitored ones.

Fig. 10 compares the simulated settlement evolution at the monitoring point V2-3 in the middle of the maximum cross section with the monitored data. It demonstrates that the calculated settlement evolution at the point V2-3 agrees basically with the monitored one with a significant increase during the construction and an insignificant increase under the action of the water filling. As the creep deformation of the rockfills was not taken into account in the calculation, the calculated settlement-time curve was slightly lower than the monitored one in Fig. 10.

Fig. 11 shows the comparison of the calculated dam settlement with the monitored data along the longitudinal section V-V after the first impounding. The settlement values are presented in the form of fractional numbers beside the monitoring points, in which the numerator and the denominator denote the monitored values and the calculated values, respectively. It can be seen that the calculated settlement at each monitoring point (VC1 to VC8) is close to the monitored one. The calculated maximum settlement occurs nearly in the middle of the dam height at the maximum section. As we know, for the dam built directly on rock foundations, the maximum settlement of the dam would occur at nearly 2/3 dam height. In the calculated project, the dam was built on an alluvium foundation as shown in Fig. 4. The weight of the dam body and the water pressure will induce the settlement deformation of the alluvium foundation, leading to the downward movement of the location for the maximum settlement of the dam body. So, the maximum settlement of the dam body shown in Figs. 7(a) and 11 occur nearly in the middle of the dam height, as reported in [42–44].

In this rockfill dam, the horizontal displacements on the downstream slope have been monitored with a relatively high accuracy. The monitored horizontal displacements after the first impounding agree roughly with the calculated ones, as shown in Fig. 12. The maximum horizontal displacement occurred near the 2/3-height of the dam. Along the dam height, the distribution of the horizontal displacements on the downstream slope is similar to that of the deflections of the face slabs.

In summary, both the calculated deformation of the dam body and the deflection of the concrete face slabs agree roughly with the

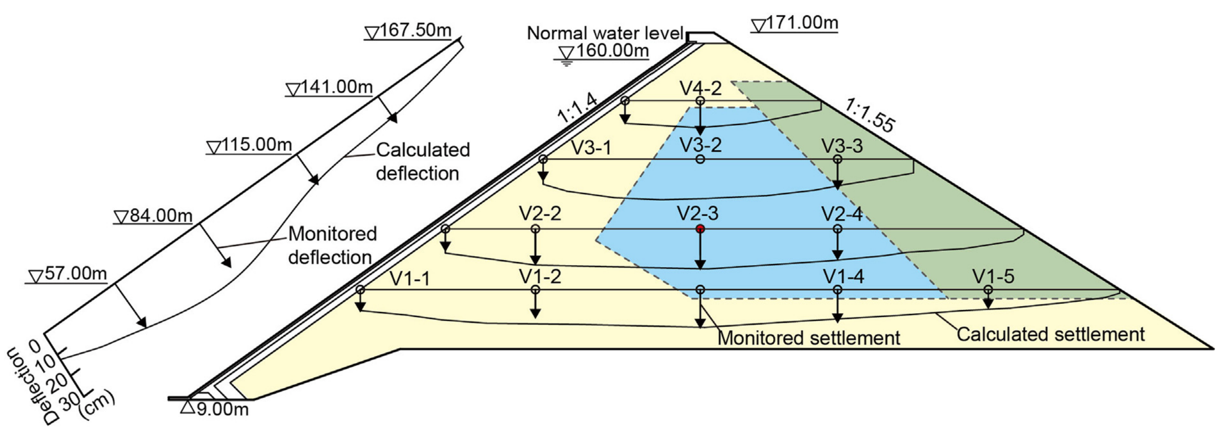

Fig. 9. Comparison of the numerically calculated dam settlement and the slab deflection with the measurement at the maximum cross section after the first impounding.

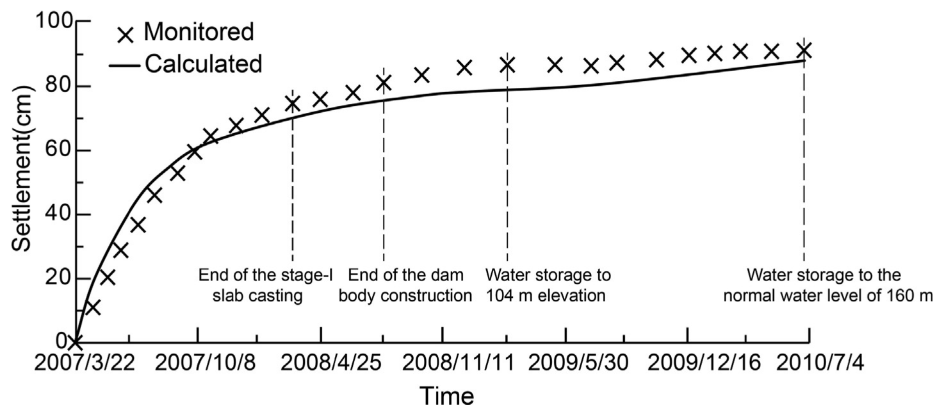

Fig. 10. Settlement–time curves at the monitoring point V2-3.

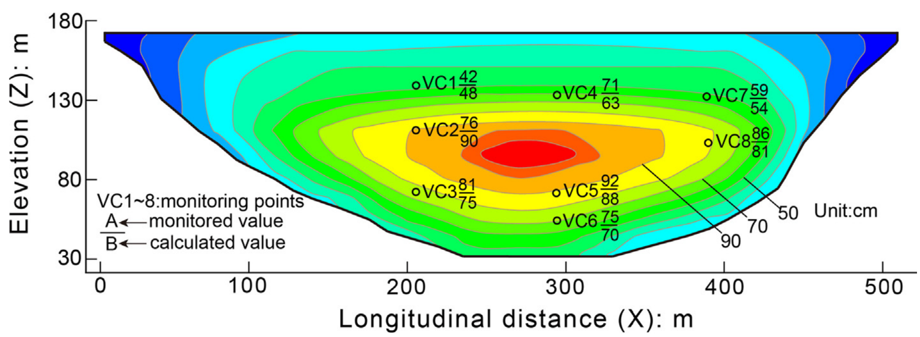

Fig. 11. Comparison of the calculated dam body settlement with the measurement along the longitudinal section V-V after the first impounding.

monitored ones, indicating the rationality of the proposed nonlinear constitutive model for rockfill materials.

4. Conclusions

(1) A nonlinear constitutive model for rockfill materials that can reflect the coupling influence of the mean effective stress p and the deviatoric stress q on the deformation of rockfill materials was proposed. The model is of simple form but can account for the dilatancy behavior, the strength nonlinearity of rockfill materials as well as the influence of the intermediate principal stress. There are 10 parameters involved in the model, which can be determined by conventional tests.

(2) The validity of this nonlinear constitutive model was verified by modelling the triaxial tests on 6 kinds of rockfill materials used in the Tankeng CFRD. This model was confirmed to be effective in reproducing basic features of rockfill materials, such as volumetric change due to dilatancy and a nonlinear frictional behavior.

(3) This model was applied in the 3D FE calculation for the Tankeng CFRD. The calculated deformation of the dam body and the deflection of the concrete face slabs are in good agreement with the in-situ measurements, indicating that the proposed model could easily implemented in a 3D FE simulation and is able to capture the main mechanical responses of rockfill materials in a rockfill dam.

Acknowledgements

This work was supported by the “National Key R&D Program of China” (Grant No. 2017YFC0404800), and the “National Natural Science Foundation of China” (Grant Nos. U1765205 and 51979091).

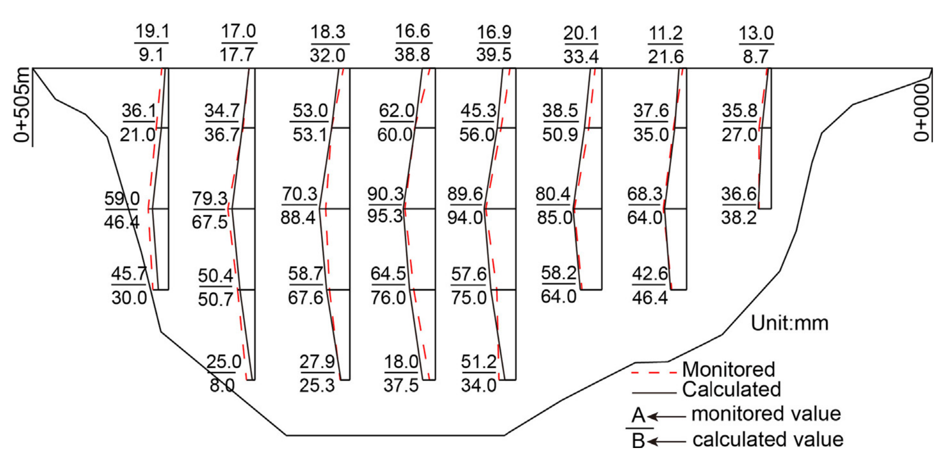

Fig. 12. Comparison of the calculated horizontal displacements with the monitored ones on the downstream slope after the first impounding.

Appendix A

In FE calculation, the constitutive model established in *p-q* stress space should be expressed in Voigt stress space.

Eq. (1) is rewritten as

$$d\sigma_{ij} = D_{ijkl}(\sigma_{mn})d\varepsilon_{kl} \tag{A.1}$$

where D_{ijkl} is the inverse of C_{ijkl} that are stress level dependent. Under the isotropic condition, D_{ijkl} can be expressed as

$$\begin{aligned} D_{ijkl}(\sigma_{mn}) = {} & A_1\delta_{ij}\delta_{kl} + A_2(\delta_{ik}\delta_{jl} + \delta_{jk}\delta_{il}) + A_3\sigma_{ij}\delta_{kl} + A_4\delta_{ij}\sigma_{kl} + A_5(\delta_{ik}\sigma_{jl} + \delta_{il}\sigma_{jk} + \delta_{jk}\sigma_{il} + \\ & \delta_{jl}\sigma_{ik}) + A_6\delta_{ij}\sigma_{km}\sigma_{ml} + A_7\delta_{kl}\sigma_{im}\sigma_{mj} + A_8(\delta_{ik}\sigma_{jm}\sigma_{ml} + \delta_{il}\sigma_{jm}\sigma_{mk} + \delta_{jk}\sigma_{im}\sigma_{ml} + \\ & \delta_{jl}\sigma_{im}\sigma_{mk}) + A_9\sigma_{ij}\sigma_{kl} + A_{10}\sigma_{ij}\sigma_{km}\sigma_{mi} + A_{11}\sigma_{im}\sigma_{mj}\sigma_{kl} + A_{12}\sigma_{im}\sigma_{mj}\sigma_{kn}\sigma_{nl} \end{aligned} \tag{A.2}$$

where A_1, A_2, $\cdots$,A_{12} are coefficients related to stress invariants, and δ is the Kronecker delta (when $i = j$, $\delta_{ij} = 1$; when $i \neq j$, $\delta_{ij} = 0$). It is assumed that the coefficients A_5 to A_{12} are related to higher-order stress invariants and their values equal zero. Then Eq. (A.2) can be simplified as

$$D_{ijkl}(\sigma_{mn}) = A_1\delta_{ij}\delta_{kl} + A_2(\delta_{ik}\delta_{jl} + \delta_{jk}\delta_{il}) + A_3\sigma_{ij}\delta_{kl} + A_4\delta_{ij}\sigma_{kl} \tag{A.3}$$

Substituting Eq. (A.3) into Eq. (A.1) yields

$$d\sigma_{ij} = A_1\delta_{ij}d\varepsilon_{kk} + 2A_2d\varepsilon_{ij} + A_3\sigma_{ij}d\varepsilon_{kk} + A_4\delta_{ij}\sigma_{kl}d\varepsilon_{kl} \tag{A.4}$$

Under the triaxial stress state, Eq. (A.4) can be expressed as

$$\left.\begin{array}{r} d\sigma_{11} = A_1d\varepsilon_{kk} + 2A_2d\varepsilon_{11} + A_3\sigma_{11}d\varepsilon_{kk} + A_4(\sigma_{11}d\varepsilon_{11} + 2\sigma_{22}d\varepsilon_{22}) \\ d\sigma_{22} = A_1d\varepsilon_{kk} + 2A_2d\varepsilon_{22} + A_3\sigma_{22}d\varepsilon_{kk} + A_4(\sigma_{11}d\varepsilon_{11} + 2\sigma_{22}d\varepsilon_{22}) \\ d\sigma_{33} = d\sigma_{22} \qquad\qquad\qquad\qquad \end{array}\right\} \tag{A.5}$$

and the increments of p, q, ε_v and ε_s can be written as

$$\left.\begin{array}{r} dp = \frac{(d\sigma_{11} + 2d\sigma_{33})}{3} \\ dq = d\sigma_{11} - d\sigma_{33} \\ d\varepsilon_v = d\varepsilon_{11} + 2d\varepsilon_{33} \\ d\varepsilon_s = \frac{2}{3}(d\varepsilon_{11} - d\varepsilon_{33}) \end{array}\right\} \tag{A.6}$$

Combining Eq. (A.5) and Eq. (A.6) yields

$$\left.\begin{array}{l} dp = \left(A_1 + \frac{2}{3}A_2 + pA_3 + pA_4\right)d\varepsilon_v + A_4qd\varepsilon_s \\ dq = A_3qd\varepsilon_v + 3A_2d\varepsilon_s \end{array}\right\} \tag{A.7}$$

The inverse expression of Eq. (3) can be written as

$$\left.\begin{array}{l} dp = \bar{K}d\varepsilon_v - \bar{J}d\varepsilon_s \\ dq = -\bar{J}d\varepsilon_v + \bar{G}d\varepsilon_s \end{array}\right\} \tag{A.8}$$

where moduli $\bar{K}$, $\bar{J}$, $\bar{G}$ can be represented by K, J, G as follows

$$\left.\begin{array}{r} \bar{K} = K\frac{J^2}{J^2 - KG} \\ \bar{G} = G\frac{J^2}{J^2 - KG} \\ \bar{J} = \frac{KGJ}{J^2 - KG} \end{array}\right\} \tag{A.9}$$

From Eqs. (A.7) and Eq. (A.8), coefficients A_1–A_4 can be obtained

$$\left.\begin{array}{r} A_1 = \bar{K} - \frac{2}{9}\bar{G} + \frac{2p}{q}\bar{J} \\ A_2 = \frac{\bar{G}}{3} \\ A_3 = A_4 = -\frac{\bar{J}}{q} \end{array}\right\} \tag{A.10}$$

Substituting Eq. (A.10) into Eq. (A.4) yields

$$d\sigma_{ij} = \left(\bar{K} - \frac{2}{9}\bar{G} + \frac{2p}{q}\bar{J}\right)\delta_{ij}d\varepsilon_{kk} + \frac{2}{3}\bar{G}d\varepsilon_{ij} - \frac{\bar{J}}{q}\sigma_{ij}d\varepsilon_{kk} - \frac{\bar{J}}{q}\delta_{ij}\sigma_{kl}d\varepsilon_{kl} \tag{A.11}$$

Eq. (A.11) is the expression of stress-strain relationship in Voigt stress space, which can also be written in a matrix form

$$\{d\sigma\} = [D]\{d\varepsilon\} \tag{A.12}$$

which can be expanded as

$$\begin{Bmatrix} d\sigma_{11} \\ d\sigma_{22} \\ d\sigma_{33} \\ d\sigma_{12} \\ d\sigma_{23} \\ d\sigma_{31} \end{Bmatrix} = \begin{bmatrix} D_{11} & D_{12} & D_{13} & D_{14} & D_{15} & D_{16} \\ D_{21} & D_{22} & D_{23} & D_{24} & D_{25} & D_{26} \\ D_{31} & D_{32} & D_{33} & D_{34} & D_{35} & D_{36} \\ D_{41} & D_{42} & D_{43} & D_{44} & 0 & 0 \\ D_{51} & D_{52} & D_{53} & 0 & D_{55} & 0 \\ D_{61} & D_{62} & D_{63} & 0 & 0 & D_{66} \end{bmatrix} \begin{Bmatrix} d\varepsilon_{11} \\ d\varepsilon_{22} \\ d\varepsilon_{33} \\ d\gamma_{12} \\ d\gamma_{23} \\ d\gamma_{31} \end{Bmatrix} \tag{A.13}$$

where $[D]$ is a symmetric stiffness matrix, and items in the matrix can be expressed as

$$\left.\begin{array}{c} D_{11} = \alpha_1 + 2\alpha_3;\ D_{12} = D_{21} = \alpha_2 + \alpha_3 + \alpha_4 \\ D_{22} = \alpha_1 + 2\alpha_4;\ D_{23} = D_{32} = \alpha_2 + \alpha_4 + \alpha_5 \\ D_{33} = \alpha_1 + 2\alpha_5;\ D_{31} = D_{13} = \alpha_2 + \alpha_3 + \alpha_5 \\ D_{44} = D_{55} = D_{66} = \frac{\bar{G}}{3} \\ D_{41} = D_{42} = D_{43} = D_{14} = D_{24} = D_{34} = \frac{-J\sigma_{12}}{q} \\ D_{51} = D_{52} = D_{53} = D_{15} = D_{25} = D_{35} = \frac{-J\sigma_{23}}{q} \\ D_{61} = D_{62} = D_{63} = D_{16} = D_{26} = D_{36} = \frac{-J\sigma_{31}}{q} \end{array}\right\} \tag{A.14}$$

in which

$$\left.\begin{array}{c} \alpha_1 = \bar{K} + \frac{4}{9}\bar{G} \\ \alpha_2 = \bar{K} - \frac{2}{9}\bar{G} \\ \alpha_3 = \frac{J}{3q}(\sigma_{22} + \sigma_{33} - 2\sigma_{11}) \\ \alpha_4 = \frac{J}{3q}(\sigma_{11} + \sigma_{33} - 2\sigma_{22}) \\ \alpha_5 = \frac{J}{3q}(\sigma_{22} + \sigma_{11} - 2\sigma_{33}) \end{array}\right\} \tag{A.15}$$

References

[1] El Dine BS, Dupla JC, Frank R, Canou J, Kazan Y. Mechanical characterization of matrix coarse-grained soils with a large-sized triaxial device. Can Geotech J 2010;47(4):425–38.
[2] Xiao Y, Liu H, Chen Y, Jiang J, Zhang W. Testing and modeling of the state-dependent behaviors of rockfill material. Comput Geotech 2014;61:153–65.
[3] Xiao Y, Liu H, Chen Y, Jiang J. Strength and deformation of rockfill material based on large-scale triaxial compression tests. I: Influences of density and pressure. J Geotech Geoenviron Eng 2014;140(12):04014070.
[4] Xiao Y, Liu H, Liu H, Chen Y, Zhang W. Strength and dilatancy behaviors of dense modeled rockfill material in general stress space. Int J Geomech 2016;16(5):04016015.
[5] Duncan JM, Chang CY. Nonlinear analysis of stress and strain in soils. J Soil Mech Found Div, ASCE 1970;96(SM5):1629–53.
[6] Domaschuk L, Villiappan P. Nonlinear settlement analysis by finite element. J Geotech Geoenviron Eng 1975;101(7):601–14.
[7] Darve F, Labanieh S. Incremental constitutive law for sands and clays: simulations of monotonic and cyclic tests. Int J Numer Anal Methods Geomech 1982;6(2):243–75.
[8] Darve F, Flavigny E, Meghachou M. Yield surfaces and principle of superposition: revisit through incrementally non-linear constitutive relations. Int J Plasticity 1995;11(8):927–48.
[9] Roscoe KH, Schofield AN, Wroth CP. On the yielding of soils. Géotechnique 1958;8(1):22–53.
[10] Gajo A, Muir Wood D. A kinematic hardening constitutive model for sands: the multiaxial formulation. Int J Numer Anal Methods Geomech 1999;23(9):925–65.
[11] Yao YP, Sun DA, Matsuoka H. A unified constitutive model for both clay and sand with hardening parameter independent on stress path. Comput Geotech 2008;35(2):210–22.
[12] Yao YP, Hou W, Zhou AN. UH model: three-dimensional unified hardening model for overconsolidated clays. Geotechnique 2009;59(5):451–69.
[13] Kong Y, Xu M, Song E. An elastic-viscoplastic double-yield-surface model for coarse-grained soils considering particle breakage. Comput Geotech 2017;85:59–70.
[14] Yao YP, Liu L, Luo T. A constitutive model for granular soils. Sci China Tech Sci 2018;61(10):1546–55.
[15] Yang ZX, Xu TT, Li XS. J2-deformation type model coupled with state dependent dilatancy. Comput Geotech 2019;105:129–41.
[16] Liu SH, Shen CM, Mao HY, Sun Y. State-dependent elastoplastic constitutive model for rockfill materials. Rock Soil Mech 2019;40(8):2891–8. [in Chinese].
[17] Yao YP, Liu L, Luo T, Tian Y, Zhang JM. Unified hardening (UH) model for clays and sands. Comput Geotech 2019;110:326–43.
[18] Niemunis A, Herle I. Hypoplastic model for cohesionless soils with elastic strain range. Mech Cohes-Frict Mater 1997;2(4):279–99.
[19] Maier T. Nonlocal modeling of softening in hypoplasticity. Comput Geotech 2003;30(7):599–610.
[20] Weifner T, Kolymbas D. A hypoplastic model for clay and sand. Acta Geotech 2007;2(2):103–12.
[21] Mašín D. Hypoplastic Cam-clay model. Géotechnique 2012;62(6):549–53.
[22] Chang CS, Hicher PY. An elasto-plastic model for granular materials with microstructural consideration. Int J Solids Struct 2005;42(14):4258–77.
[23] Yin ZY, Chang CS, Hicher PY. Micromechanical modelling for effect of inherent anisotropy on cyclic behaviour of sand. Int J Solids Struct 2010;47(14–15):1933–51.
[24] Yin ZY, Zhao JD, Hicher PY. A micromechanics-based model for sand-silt mixtures. Int J Solids Struct 2014;51(6):1350–63.
[25] Shen CM, Liu SH, Wang LJ, Wang YS. Micromechanical modeling of particle breakage of granular materials in the framework of thermomechanics. Acta Geotech 2019;14(4):939–54.
[26] Yin JH, Saadat F, Graham J. Constitutive modelling of a compacted sand–bentonite mixture using three-modulus hypoelasticity. Can Geotech J 1990;27(3):365–72.
[27] Sun T, Gao XZ. Containing dilatancy and strain softening of earth's K-G model. Rock Soil Mech 2005;26(9):1369–73. [in Chinese].
[28] Cheng ZL, Jiang JS, Ding HS, Zuo YZ. Nonlinear dilatancy model for coarse-grained soils. Chin J Geotech Eng 2010;32(3):460–7. [in Chinese].
[29] Sun DA, Huang WX, Sheng DC, Yamamoto H. An elastoplastic model for granular materials exhibiting particle crushing. Key Eng Mater 2007;340–341:1273–8.
[30] Janbu N. Soil compressibility as determined by oedometer and triaxial tests. Proceedings of the European conference on soil mechanics and foundation engineering, Wiesbaden. 1963. p. 19–25.
[31] Matsuoka H. On the significance of the spatial mobilized plane. Soils Found 1976;16(1):91–100.
[32] Matsuoka H, Yao YP, Sun DA. The Cam-clay models revised by the SMP criterion. Soils Found 1999;39(1):81–95.
[33] Liu SH, Shao DC, Shen CM, Wan ZJ. A microstructure-based elastoplastic constitutive model for coarse-grained materials. Chin J Geotech Eng 2017;39(5):777–83. [in Chinese].
[34] Pastor M, Zienkiewicz OC, Chan AHC. Generalized plasticity and the modelling of soil behaviour. Int J Numer Anal Methods Geomech 1990;14(3):151–90.
[35] Wang ZJ, Liu SH, Vallejo L, Wang LJ. Numerical analysis of the causes of face slab cracks in Gongboxia rockfill dam. Eng Geol 2014;181:224–32.
[36] Wen LF, Chai JR, Xu ZG, Qin Y, Li YL. Monitoring and numerical analysis of behaviour of miaojiaba concrete-face rockfill dam built on river gravel foundation in china. Comput Geotech 2017;85:230–48.
[37] Wen LF, Chai JR, Xu ZG, Qin Y, Li YL. A statistical review of the behaviour of concrete face rockfill dams based on case histories. Géotechnique 2018;68(9):1–61.
[38] Sukkarak R, Pramthawee P, Jongpradist P, Kongkitkul W, Jamsawang P. Deformation analysis of high CFRD considering the scaling effects. Comput Geotech 2018;14(3):211–24.
[39] Goodman RE, Taylor RL, Brekke TL. A model for the mechanics of jointed rock. J Soil Mech Found Div, ASCE 1968;94(SM 3):637–59.

[40] Clough GW, Duncan JM. Finite element analyses of retaining wall behavior. J Soil Mech Found Div, ASCE 1971;97(SM 12):1657–72.
[41] Qu Y, Zou D, Kong X, Xu B. A novel interface element with asymmetric nodes and its application on concrete-faced rockfill dam. Comput Geotech 2017;85:103–16.
[42] Özkuzukiran S, Özkan MY, Özyazicioğlu M, Yildiz GS. Settlement behaviour of a concrete faced rock-fill dam. Geotech Geol Eng 2006;24(6):1665–78.
[43] Zhou W, Hua J, Chang X, Zhou C. Settlement analysis of the Shuibuya concrete-face rockfill dam. Comput Geotech 2011;38(2):269–80.
[44] Xu B, Zou D, Liu H. Three-dimensional simulation of the construction process of the Zipingpu concrete face rockfill dam based on a generalized plasticity model. Comput Geotech 2012;43:143–54.